Nonreciprocal Elastic Wave Beaming in Dynamic Phased Arrays

M. Moghaddaszadeh[1,2], R. Adlakha[2], M. A. Attarzadeh[2], A. Aref[1], and M. Nouh[2]*

[1] *Dept. of Civil, Structural and Environmental Engineering, University at Buffalo (SUNY), Buffalo, NY 14260-4300*
[2] *Dept. of Mechanical and Aerospace Engineering, University at Buffalo (SUNY), Buffalo, NY 14260-4400*

(Dated: August 28, 2021)

Beam forming using phased arrays forms the basis of several sonar communication and biomedical imaging techniques. However, to date, such arrays remain constrained by wave reciprocity in addition to being confined to their operational frequency; two limitations which have severely hindered imaginative advancements in this domain. In the context of sound propagation, nonreciprocity typically refers to unidirectional elastic and surface acoustic wave devices. However, a breakage of reciprocity in phased arrays manifests itself in reception and transmission patterns which can be independently tuned; which has thus far been elusive. This work reports on a class of nonreciprocal phased arrays which operate independently and simultaneously within different directions and frequency channels, thus breaking transmission-reception symmetry and offering enhanced capabilities in guided wave engineering. The array comprises an array of transceiving piezoelectric wafer discs bonded to an elastic medium and incorporates a prescribed dynamic modulation on top of a static phase gradient, which enables concurrent phononic transitions in energy and momentum spaces that mitigate the constraints imposed by Lorentz reciprocity. Following the theory and predictive analysis, the entire array and its associated capabilities are demonstrated experimentally.

I. INTRODUCTION

Guided elastic waves have been a cornerstone of structural health monitoring and nondestructive testing for decades owing to their superior sensitivity to defects [1–3]. They have also been adopted in medical applications due to their low damping, allowing them to travel long distances without dissipation [4], and to manipulate the direction of incident waves via diffraction gratings [5, 6] and metasurfaces [7]. As one of the most prevalent methods for guided wave engineering, surface-mounted piezoelectric arrays allow efficient wave beaming [8] and sensing [9] in one self-contained configuration. Phased arrays are a union of multiple wave transmitting/receiving elements (*transceivers*) arranged in one (linear), two (planar), or three (hemispherical) dimensional configurations [10, 11]. Conventional phased arrays can transmit elastic waves in a desired direction via constructive and destructive interferences between the emitted wave fields from different array elements. The augmented phase of the individual elements can be controlled to instigate wave beaming in transmission and reception in 2D/3D spaces without requiring moving mechanical parts [12]. For example, by incorporating a quasi-statically changing phase gradient, existing phased arrays are capable of electronically steering a wave beam across the whole field of view [13]. Alternatively, by carefully designing the spatial distribution of their phase gradients, phased arrays can be used to focus wave energy at a specific point and create standing waves to trap particles or levitate objects [14]. In offering a wide portfolio of wave forming capabilities, phased arrays provide a versatile platform which can be exploited in a wide range of acoustic engineering applications [15–17]. Notable among these are fault detection in elastic media [18–21], identification of pipe damage [22, 23], wind sensing [24], and more recently, in creating high resolution 3D images of internal structural defects [25]. Nonlinear sub-harmonics and higher-harmonic ultrasonic phased arrays are now being proposed for imaging of internal closed cracks [26–28]. In the latter, however, all nonlinear harmonics ought to be received by a single phased array to obtain all the images needed and detect the open and closed portions of a crack. A traditional ultrasonic phased arrays, which can only operate in a single channel, is simply incapable of fulfilling this objective [29]. Recently, fundamental wave amplitude difference (FAD) was suggested that uses both fixed- [30–32] and different-voltage [33, 34] approaches to address this issue by measuring the incident amplitude-dependence of the fundamental wave component. Nevertheless, a more robust and straightforward strategy remains of great interest and can potentially reshape the future course of experimental structural health evaluation.

Reciprocity is one of the fundamental principles of wave propagation that often constrains the operation of phased arrays. It implies that transmission between two spatially separated locations in linear time-invariant (LTI) systems remains the same with an interchange of the actuating and sensing points [35]. An intentional breakage of this constraint opens up untapped opportunities and has understandably found applications in various fields of engineering ranging from electromagnetics [36–39], to acoustics [40–45] and elasticity [46–49]. The injection of prescribed temporal variations in systems with a spatial-gradient (with the intention of breaking time-reversal symmetry) has been demonstrated as a favorable approach due to its independence on signal intensity and its ability to be replicated in a finite prac-

* Corresponding author: mnouh@buffalo.edu

tical setting [50–52]. There are a number of studies pertaining to photonic metasurfaces, where a nonreciprocal behavior is observed by incorporating a space-time-periodic (STP) modulation of properties [53–56]. However, there are very few efforts of electromagnetic phased arrays which integrate such modulations with the underlying gradient [57]. The concept of nonreciprocity is often narrowly used to describe unidirectional wave propagation and diode-like systems. Owing to reciprocal symmetry, existing phased arrays are sensitive only to incident waves arriving from the same exact direction as those it can transmit to; a phenomenon which effectively guarantees identical radiation and reception patterns [58]. As a result, the notion of nonreciprocity in phased array platforms potentially manifests itself in the form of non-identical radiation and reception beam forming patterns, which can be independently tuned [59, 60].

This work presents a class of phased arrays which operate independently and simultaneously within different directions and frequency channels, thus breaking transmission-reception symmetry and offering superior capabilities in guided wave engineering. In the elastic domain, the experimental realization of such a system has thus far been elusive [61]. Without loss of generality, the array is comprised of an array of transceiving piezoelectric wafer discs (PWDs) which undergo dynamic phase modulation on top of a static phase gradient. Contrary to conventional arrays, the proposed system incorporates a dynamic modulation on top of the underlying static phase gradient resulting in a modified time-delay law which brings about two unprecedented functions: (1) A capability to generate several beams which can be steered independently (i.e., multiple momentum channels). (2) In the absence of advanced (and often time-consuming) accommodations to operate within wide-band and nonlinear regimes, the system presented here invokes multiple frequency channels that can be each individually tuned such that all required data can be derived with a single measurement without the need for any sub/super-harmonic post processing schemes. The combined multiple momentum and frequency channels within the array not only prompt faster scanning (as the time required to scan the complete domain is inversely proportional to the number of simultaneous momentum channels), but also enables concurrent measurements of distinct frequency content for different channels in both transmission and reception operations. Finally, we report on the array's capability of inducing increasingly nonreciprocal radiation and reception patterns *in situ*. The entire array and its associated capabilities are demonstrated experimentally, confirming the theoretical framework established here and setting a road map for broader future implementation.

II. THEORY OF DYNAMIC ELASTOACOUSTIC PHASED ARRAY

The proposed STP-PWD phased array breaks time-reversal symmetry via a space-time-variation of phase gradient, which selectively alters directional and frequency content of various harmonics generated by the array, as illustrated in Fig. 1. A transceiver of the proposed phased array comprises a single PWD coupled with a phase-shifter. Consider a dynamic phase angle for the n^{th} PWD of the following STP form

$$\phi_n(t) = \kappa_c y_n + \delta \cos(\omega_m t - \kappa_m y_n) \tag{1}$$

where y_n is the y-coordinate of the n^{th} PWD along the array as depicted in Fig. 1(a). κ_c is the static phase gradient (also present in conventional phased arrays), δ denotes the STP modulation depth, ω_m and κ_m are the temporal and spatial modulation frequencies, respectively. The figure also shows the array with N PWDs surface-mounted on a thin plate and linearly distributed with a pitch d.

A. Transmission

When transmitting, the array is excited with an input voltage of the form $V_0 \mathrm{e}^{-\mathrm{i}\omega t}$, where V_0 is the amplitude, $\mathrm{i} = \sqrt{-1}$, and ω is the temporal frequency. Subsequently, each phase-shifter augments this signal with the STP phase angle described by Eq. (1), $v_n(t) = V_0\, \mathrm{e}^{\mathrm{i}[-\omega t + \phi_n(t)]}$. The supplied voltage to the n^{th} PWD, thus becomes

$$v_n(t) = V_0\, \mathrm{e}^{\mathrm{i}(-\omega t + \kappa_c y_n)}\, \mathrm{e}^{\mathrm{i}\delta \cos(\omega_m t - \kappa_m y_n)} \tag{2}$$

Using the Jacobi-Anger expansion, this can be replaced with an infinite series of Bessel functions. Upon further simplification, we get

$$v_n(t) = V_0 \sum_{q=-\infty}^{\infty} \mathrm{i}^q \mathbb{J}_q(\delta)\, \mathrm{e}^{\mathrm{i}(-\omega^{(q)} t + \kappa_c^{[q]} y_n)} \tag{3}$$

where $\mathbb{J}_q(\bullet)$ is a q^{th}-order Bessel function of the first kind and $(\bullet)^{(q)}$ and $(\bullet)^{[q]}$ are shorthand notations for a frequency shift of $+q\omega_m$ and a phase gradient shift of $+q\kappa_m$, respectively, i.e., $\omega^{(q)} = \omega + q\omega_m$ and $\kappa_c^{[q]} = \kappa_c + q\kappa_m$. Applying this voltage to the n^{th} PWD generates a radial strain which is transferred to the substrate plate through the shear coupling of bonding layer. This shear stress excitation induces Lamb waves with a displacement distribution on the top surface of the plate, $w_n(r_n, t)$. The total far-field out-of-plane displacement field is then computed by adding the field generated by the individual STP-PWDs, i.e., $w_{\text{net}}(r, t) = \sum_{n=1}^{N} w_n(r_n, t)$. Here, r is the radial distance from the center of the array to a field point and r_n is the radial distance between the center of the n^{th} PWD to the same field point as per Fig. 1(a). The total far-field out-of-plane displacement field, thus

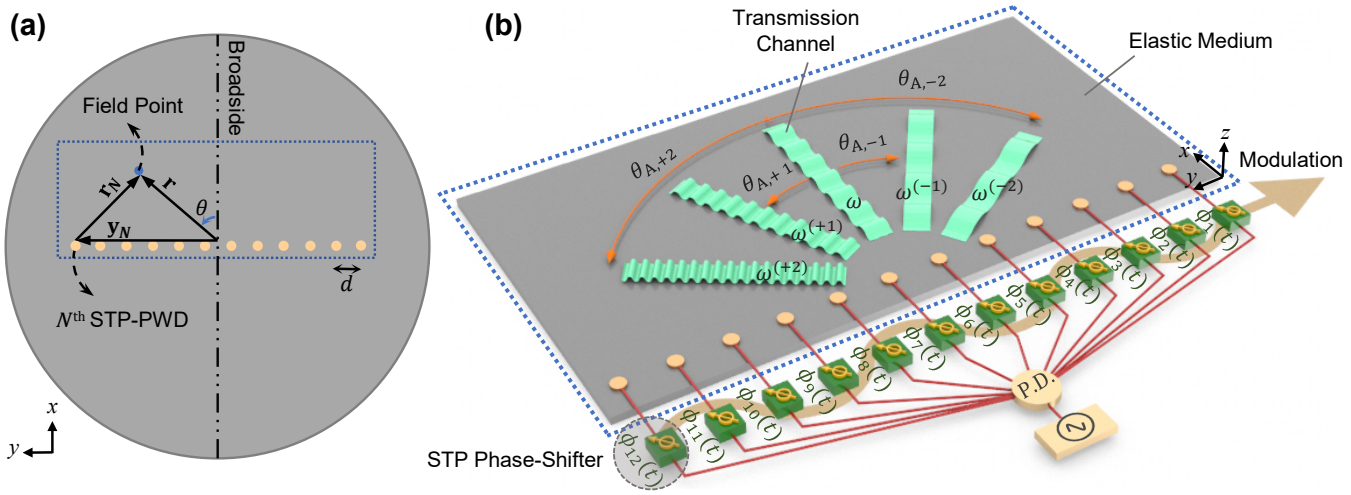

FIG. 1. **STP-PWD phased array surface-mounted on a thin aluminium plate.** (a) Coordinate system and array geometry. (b) Schematic diagram of the different array components including piezoelectric discs, STP phase-shifters, power divider (P.D.) and voltage generator. Different harmonics are generated and propagate in different directions.

becomes (See Supplementary Note 1 for a detailed derivation [62])

$$w_{\text{net}}(r,\theta,t) \cong N\mathrm{e}^{-\mathrm{i}\frac{\pi}{4}}\sqrt{\frac{2}{\pi r}}\sum_{q=-\infty}^{\infty}\left[\frac{B_{\text{S}}^{(q)}}{\sqrt{k_{\text{S}}^{(q)}}}D_{\text{S},q}(\theta)\,\psi_{\text{S}}^{(q)}(r,t) + \frac{B_{\text{A}}^{(q)}}{\sqrt{k_{\text{A}}^{(q)}}}D_{\text{A},q}(\theta)\,\psi_{\text{A}}^{(q)}(r,t)\right] \tag{4}$$

where (r,θ) are the polar coordinates of a field point of interest with respect to the center of the array, while θ is measured counter-clockwise from broadside, as shown in Fig. 1(a). $k_\alpha^{(q)}$ is the frequency-shifted wavenumber of the first symmetric (or antisymmetric) Lamb wave, for $\alpha = \text{S}$ (or $\alpha = \text{A}$), and $B_\alpha^{(q)}$ is the associated amplitude coefficient (See Supplementary Note 1 for more details). In Eq. (4), $\psi_\alpha^{(q)}(r,t) = \mathrm{e}^{\mathrm{i}(-\omega^{(q)}t + k_\alpha^{(q)}r)}$ denotes a symmetric (for $\alpha = \text{S}$) or antisymmetric (for $\alpha = \text{A}$) spherical Lamb wave with a unit amplitude. Due to the elliptical motion of material particles in both symmetric and antisymmetric Lamb waves, the two are naturally coupled and Eq. (4) confirms that they appear alongside one another in out-of-plane deformations. Further, $D_{\alpha,q}(\theta)$ represents q^{th}-order modified transmission directivities of the array for the first symmetric and antisymmetric Lamb waves as follows

$$D_{\alpha,q}(\theta) = \mathrm{i}^q\mathbb{J}_q(\delta)\frac{\sin\left[\frac{Nd}{2}(k_\alpha^{(q)}\sin\theta - \kappa_c^{[q]})\right]}{N\sin\left[\frac{d}{2}(k_\alpha^{(q)}\sin\theta - \kappa_c^{[q]})\right]};\quad \alpha = \text{S},\text{A} \tag{5}$$

An inspection of Eq. (4) and $\psi_\alpha^{(q)}(r,t)$ reveals that in addition to the fundamental mode, an infinite set of harmonics of both first Lamb waves travel in the structure with different frequencies and wavenumbers, effectively acting as different transmission channels. The amplitude, wavenumber, and directional behavior of these channels primarily depends on the phase angle parameters and are *in situ* tunable to achieve a desired performance (see Supplementary Note 2). A q^{th}-order transmission channel, however, is not equally strong in every direction θ. Its propagation strength along any direction θ can be quantified using its $D_{\alpha,q}(\theta)$ function (see Supplementary Note 3). Practically, we are able to define principal transmission directions for both symmetric and antisymmetric Lamb waves as the θ-values which maximize the respective directivities and corresponding wave amplitudes. Using Eq. (5), we determine the q^{th}-order ($q \in \mathbb{Z}$) principal transmission directions for the first Lamb waves to be $\theta_{\alpha,q} = \sin^{-1}(\kappa_c^{[q]}/k_\alpha^{(q)})$ with $\alpha = \text{S},\text{A}$. In the most general case, $k_{\text{S}}^{(q)}$ and $k_{\text{A}}^{(q)}$ can only be computed after numerically solving the symmetric and antisymmetric Rayleigh-Lamb equations for a given $\omega^{(q)}$ [63]; however, for sufficiently small values of $h\omega^{(q)}/2\pi \leq 100$ kHz·mm where h is the plate thickness, the first symmetric and antisymmetric Lamb waves asymptotically approach the behavior of extensional and flexural plate waves and $k_{\text{S,A}}$ can then be approximated accordingly [1]. As such, to facilitate an analytical solution, we limit our analysis to systems where the frequency-shifted symmetric wavenumber is $k_{\text{S}}^{(q)} = \omega^{(q)}\sqrt{\rho(1-\nu^2)/E}$ and the frequency-shifted antisymmetric wavenumber is $k_{\text{A}}^{(q)} = \sqrt{\omega^{(q)}}[12\rho(1-\nu^2)/Eh^2]^{1/4}$. Here, E is the modulus of elasticity, ν is Poisson's ratio and ρ is the plate material density. We note that the flexural waves predominantly result in out-of-plane shear deformations, while exten-

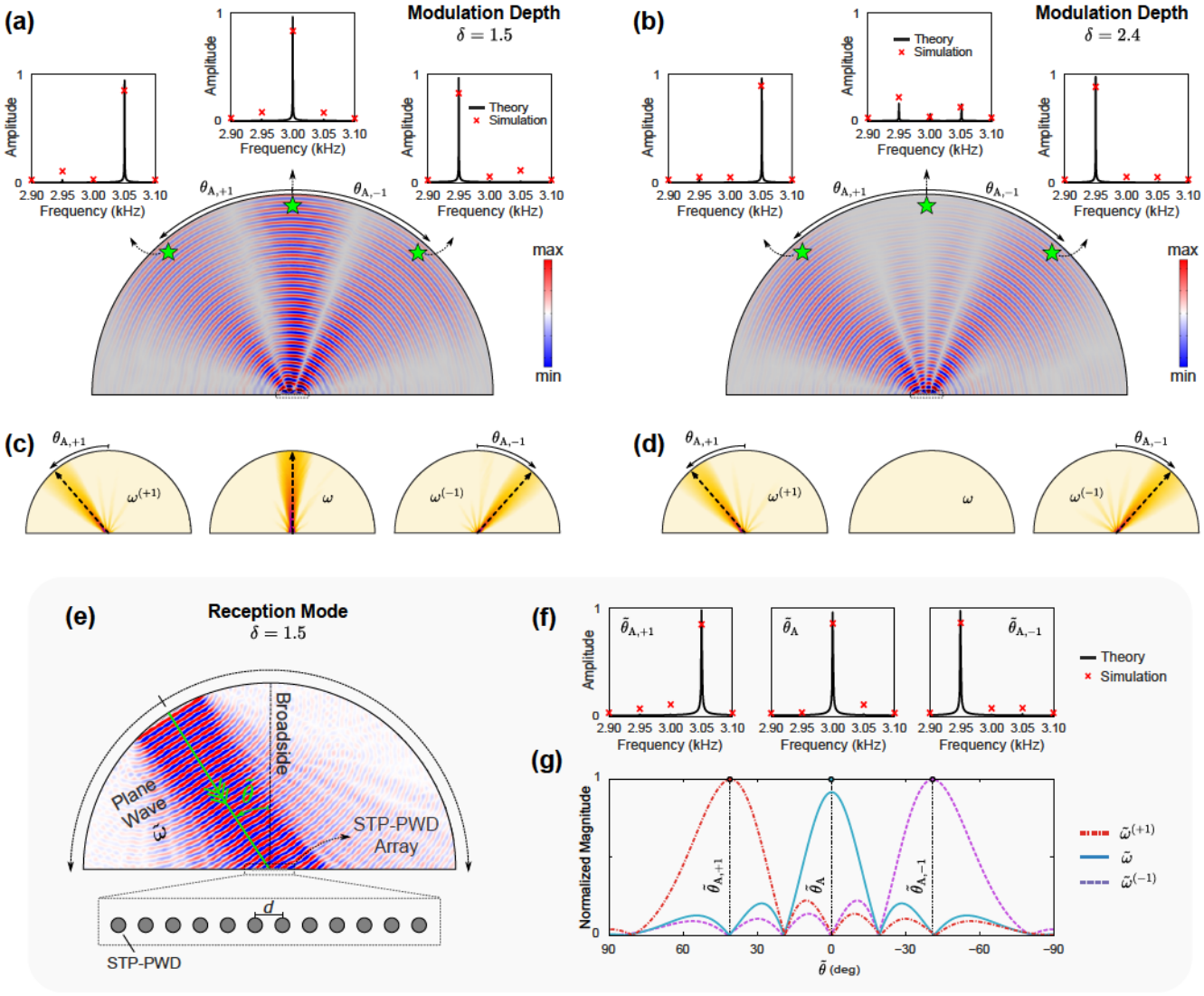

FIG. 2. **STP-PWD phased array in transmission and reception modes.** (a,b) Out-of-plane displacement field at $t = 0.005$ seconds for a modulation depth of $\delta = 1.5$ and $\delta = 2.4$, respectively. The insets show the normalized FFT amplitudes of sensor locations indicated by stars as predicted by both theory and simulations. (c,d) Directional breakdown and distribution of the FFT amplitudes for up-converted, fundamental and down-converted harmonics when $\delta = 1.5$ and $\delta = 2.4$, respectively. Theoretical principal transmission directions are plotted as dashed arrows for comparison. (e) Plane wave with frequency of $\tilde{\omega}$ incident upon the array from an arbitrary angle $\tilde{\theta}$. (f) From left to right: Normalized FFT amplitudes (both theory and simulations) of received signal at output channel when the incoming plane wave is incident from $\tilde{\theta}_{A,+1}$, $\tilde{\theta}_A$ and $\tilde{\theta}_A$, 1, respectively. (g) FFT magnitude of received signal at output channel as a function of the incident angle for different harmonics. Theoretical principal reception directions are ploted as dashed lines for comparison. Here, $\omega/2\pi = \tilde{\omega}/2\pi = 3$ kHz, $\omega^{(+1)}/2\pi = \tilde{\omega}^{(+1)}/2\pi = 3.05$ kHz, $\omega^{(-1)}/2\pi = \tilde{\omega}^{(-1)}/2\pi = 2.95$ kHz. All other parameters are defined in the Methods section.

sional waves breed in-plane displacements. As such, we focus here on out-of-plane deformations resulting from antisymmetric flexural waves in plates. The top panel of Fig. 2 illustrates the transmission behavior of the STP-PWD phased array operating at two modulation depths, $\delta = 1.5$ and $\delta = 2.4$ predicted by both theory and simulations. Here, a 6 m-radius thin circular plate ($h = 1.27$ mm thickness) was used as an elastic medium. Finite element simulations were conducted up to 0.02 seconds, which is less than the the time waves need to reach the boundaries to avoid reflections thus enabling a 0.05 kHz resolution in the frequency spectrum. The plate is made of Aluminium with the following parameters: $E = 73.1$ GPa, $\nu = 0.33$ and $\rho = 2780$ kg/m^3. The first antisymmetric Lamb wave was generated using 12 STP-PWDs each having an $a = 4$ mm radius. A quarter-wavelength pitch was used, i.e., $d = 16$ mm. The PWDs were excited with a fundamental frequency of $\omega/2\pi = 3$ kHz. The effect of STP phase-shifters was implicitly included in the voltage provided to the PWDs using the following

set of parameters: $\omega_m/2\pi = 0.05$ kHz, $\kappa_c = 0$ and $\kappa_m = 20.4808\pi$ rad/m. As a result, each group of 6 STP-PWDs constitutes one spatial unit cell with a modulation traveling velocity of $v_m = \omega_m/\kappa_m = 4.88$ m/s. As can be seen in Fig. 2(a), the displacement field captured at $t = 0.005$ seconds with $\delta = 1.5$ exhibits three distinct transmission channels, the frequency content of which is revealed using a Fast Fourier Transform (FFT). Hereafter, we omit q from the notation when $q = 0$ since the fundamental harmonic matches the excitation frequency, i.e., $\omega^{(0)} = \omega$. The normalized spectrum of the wave passing over the sensor locations indicated by the three green markers shows the fundamental harmonic ($\omega/2\pi = 3$ kHz), first up-converted harmonic ($\omega^{(+1)}/2\pi = 3.05$ kHz), and first down-converted harmonic ($\omega^{(-1)}/2\pi = 2.95$ kHz) propagating along the $\theta_{\rm A}$, $\theta_{\rm A,+1}$ and $\theta_{\rm A,-1}$ directions, respectively. It is worth noting that sensors are placed at the the principal transmission angles given by $\theta_{{\rm A},q}$ in the array's far-field, i.e., $r \geq 1$ m. The FFT amplitudes of all three sensors (obtained via finite element (FE) simulations) are in near-perfect agreement with their counterparts computed using Eq. (4) as shown in Fig. 2(a). A visualization of the same is provided in Fig. 2(c) where the spatial distribution of FFT amplitudes are presented for different harmonics, confirming the predicted principal transmission directions (superposed as dashed black lines). For a modulation depth of $\delta = 2.4$, the fundamental harmonic completely disappears as a result of its vanishing directivity ($\mathbb{J}_0(2.4) \cong 0$). This can also be confirmed by inspecting the corresponding FFT amplitudes in Figs. 2(b) and (d). Waves traveling in the broadside direction with small amplitudes are in fact side-lobes of up- and down-converted transmission channels. For the parameters chosen here, the principal transmission directions calculated for second and higher order harmonics are complex. (Specifically for $\kappa_c = 0$, $\kappa_m = 20.4808\pi$, $\omega_m/2\pi = 0.05$ kHz and $\omega/2\pi = 3$ kHz, principal transmission directions for second order harmonics are computed as $\theta_{S,-2} = -\pi/2 + {\rm i}0.257\pi$ and $\theta_{S,+2} = \pi/2 - {\rm i}0.241\pi$). The physical implication of complex angles is that these channels only propagate along the array and eventually evanesce. They do not transmit energy due to the directivity of the PWD phased array.

B. Reception

In order to investigate the STP-PWD phased array's performance characteristics in reception mode, we consider a plane Lamb wave incident upon the array from an arbitrary direction $\tilde{\theta}$ with respect to the broadside (see Fig. 2(e)). Consistent with the previous analysis, we assume a sufficiently low frequency $\tilde{\omega}$ enabling us to account for the first symmetric and antisymmetric Lamb waves only, with $\tilde{k}_{\rm S}$ or $\tilde{k}_{\rm A}$ as wavenumbers, respectively. This results in the voltage signal received by the $n^{\rm th}$ PWD at the corresponding location of $(x, y) = (0, y_n)$ of the form

$$\tilde{v}_n(t) = t_R[\tilde{B}_{\rm S}{\rm e}^{{\rm i}(-\tilde{\omega}t - \tilde{k}_{\rm S}y_n\sin\tilde{\theta})} + \tilde{B}_{\rm A}{\rm e}^{{\rm i}(-\tilde{\omega}t - \tilde{k}_{\rm A}y_n\sin\tilde{\theta})}] \quad (6)$$

where $\tilde{B}_\alpha$ is the amplitude and $\tilde{k}_\alpha$ is the incident wavenumber of symmetric ($\alpha = {\rm S}$) or antisymmetric ($\alpha = {\rm A}$) waves. The displacement-to-voltage transfer function t_R is presumed to be identical for all array elements. The signal is then fed through the STP phase-shifters, and following another Jacobi-Anger expansion, simplifies to

$$\tilde{v}_n(t) = t_R \sum_{q=-\infty}^{\infty} {\rm i}^q \mathbb{J}_q(\delta)\, {\rm e}^{{\rm i}(-\tilde{\omega}^{(q)}t + \kappa_c^{[q]}y_n)}[\tilde{B}_{\rm S}\, {\rm e}^{-{\rm i}\tilde{k}_{\rm S}\sin\tilde{\theta}y_n} + \tilde{B}_{\rm A}\, {\rm e}^{-{\rm i}\tilde{k}_{\rm A}\sin\tilde{\theta}y_n}] \quad (7)$$

Finally, the output signal from the entire array is obtained by summing up all of the individual output signals, i.e., $\tilde{v}(t) = \sum_{n=1}^{N}\tilde{v}_n(t)$ which becomes (see Supplementary Note 1)

$$\tilde{v}(t) \cong t_R N \sum_{q=-\infty}^{\infty} [\tilde{B}_{\rm S}\tilde{D}_{{\rm S},q}(\tilde{\theta}) + \tilde{B}_{\rm A}\tilde{D}_{{\rm A},q}(\tilde{\theta})]\, {\rm e}^{-{\rm i}\tilde{\omega}^{(q)}t} \quad (8)$$

where $\tilde{D}_{\alpha,q}(\tilde{\theta})$ is the $q^{\rm th}$-order modified reception directivities of the STP-PWD phased array for the first symmetric ($\alpha = {\rm S}$) and antisymmetric ($\alpha = {\rm A}$) Lamb waves; found to be

$$\tilde{D}_{\alpha,q}(\tilde{\theta}) = {\rm i}^q\mathbb{J}_q(\delta)\frac{\sin\left[\frac{Nd}{2}(\tilde{k}_\alpha\sin\tilde{\theta} - \kappa_c^{[q]})\right]}{N\sin\left[\frac{d}{2}(\tilde{k}_\alpha\sin\tilde{\theta} - \kappa_c^{[q]})\right]}; \quad \alpha = {\rm S}, {\rm A} \quad (9)$$

Eq. (9) resembles (5) albeit with wavenumbers ($\tilde{k}_\alpha$) that are not frequency-shifted. Akin to the concept of principal transmission directions, we can define the principal reception directions as the angles along which the STP-PWD phased array is most sensitive to receiving incident waves. As such, we find the $q^{\rm th}$-order principal reception directions as $\tilde{\theta}_{\alpha,q} = \sin^{-1}(\kappa_c^{[q]}/\tilde{k}_\alpha)$ with $\alpha = {\rm S}, {\rm A}$ for symmetric and antisymmetric Lamb waves. The bottom panel of Fig. 2 depicts the behavior of the array operating in reception predicted from both theory and simulations. For evaluation purposes, the array is subjected to an antisymmetric wave incident at an arbitrary angle $\tilde{\theta}$ and comprising a frequency of $\tilde{\omega}/2\pi = 3$ kHz, as shown in Fig. 2(e). The previous 12 PWDs were utilized as receiving sensors. For each incident angle $\tilde{\theta}$, the received signals from PWDs are fed through their respective STP phase-shifters and summed up at the output port. The FFT magnitudes of the array's output is provided in Fig. 2(g) as a function of $\tilde{\theta}$ for three specific harmonics: the fundamental ($\tilde{\omega}/2\pi = 3$ kHz), up-converted ($\tilde{\omega}^{(+1)}/2\pi = 3.05$ kHz), and down-converted ($\tilde{\omega}^{(-1)}/2\pi = 2.95$ kHz) channels. Owing to the linearity of the system dynamics, it immediately follows that FFT calculations can only be done at up- and down-conversions since other frequencies cannot be generated. The theoretical principal reception

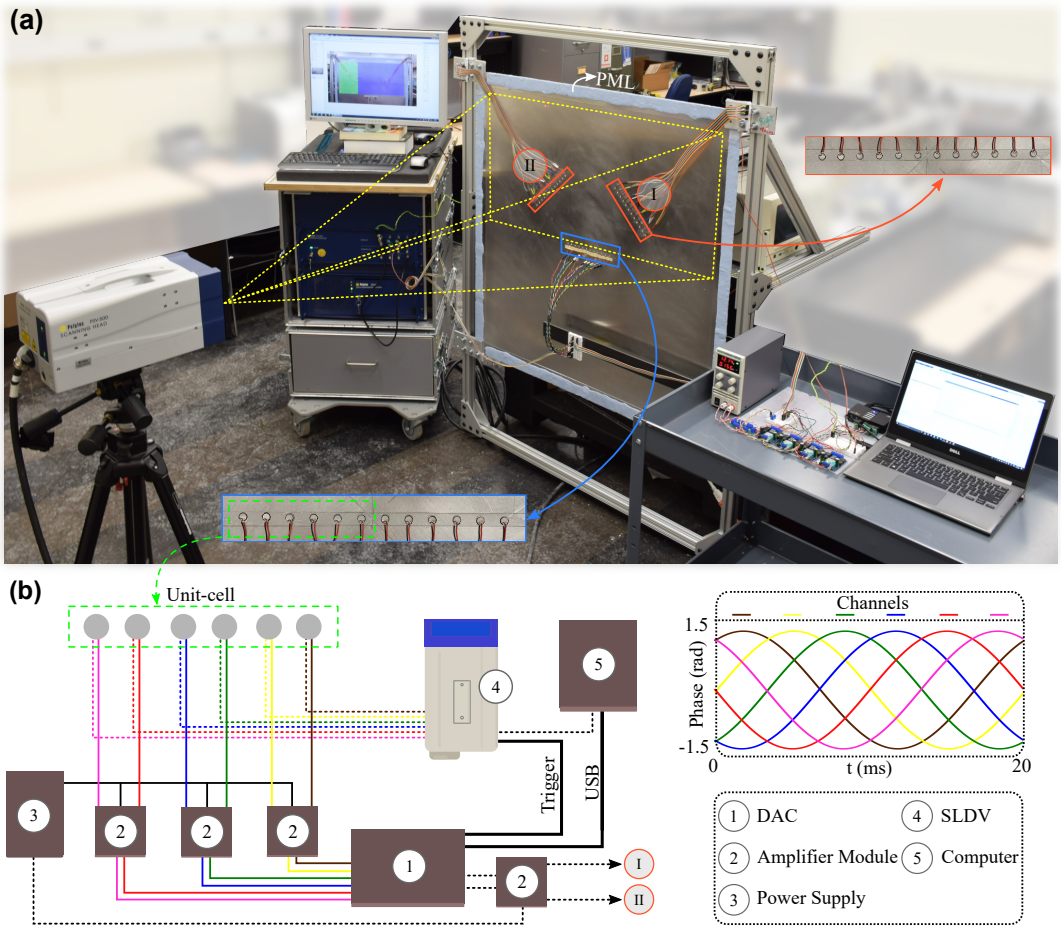

FIG. 3. **Experimental setup.** (a) Illustration of the experimental setup showing the Aluminum plate under study, mounting setup, laser vibrometer system (SLDV), controller circuit, and the perfectly matched layer (PML). The STP-PWD phased array is highlighted in the close-up using blue lines. The arrays used for generating incident waves in reception are highlighted in dashed red boxes. (b) Schematic diagram of the controller circuit. Solid lines represent the circuit for the transmission experiment, dashed lines represent the circuit for the reception experiment, and the thicker lines represent the connections that remain constant for both experiments. (I) and (II) refer to the arrays generating the different incident waves shown in (a) for the reception experiment. The individual piezoelectric connections in the schematic diagram and their respective phase signals are color-coded for clarity.

directions for first antisymmetric Lamb wave ($\tilde{\theta}_{\mathrm{A}} = 0°$, $\tilde{\theta}_{\mathrm{A},+1} = 41.4°$, and $\tilde{\theta}_{\mathrm{A},-1} = -41.4°$) are indicated on the figure as vertical dashed lines. We conclude that $\tilde{\omega}^{(q)}$ is most effectively detected with a $\tilde{\theta}_{\mathrm{A},q}$ incidence, where $q \in \mathbb{Z}$. To further elucidate this concept, Fig. 2(f) provides a comparison between the normalized FFT amplitudes of the received signal at the output channel as determined both theoretically and via FE simulations (Here, the incoming wave is incident from the exact principal reception angles for the antisymmetric wave $\tilde{\theta}_{\mathrm{A},q}$). In addition to the good agreement, we note that higher frequencies do not make a dominant appearance in the output spectrum; a phenomenon which is primarily attributed to the fact that higher harmonics do not have a real principal reception angle. For instance, the principal reception angle for the 3.10 kHz is calculated to be $\pi/2 - \mathrm{i}0.770$, and for 2.90 kHz to be $-\pi/2 + \mathrm{i}0.770$. The same can be confirmed by examining principal reception angles corresponding to higher harmonics. The nontrivial frequency conversion process taking place in an STP-PWD phased array (during reception) is significant, particularly from a practical standpoint. Conventional phased arrays quasi-statically sweep the value of κ_c to listen for omnidirectional incident waves. The proposed phased array with fixed parameters is potentially capable of the same by exploiting its reception features, specifically by only analyzing amplitudes of the various harmonics in the collected signal. If the parameters are tuned to the exact incident angles of multiple waves with the same frequency $\tilde{\omega}$, it becomes possible to clearly identify the dominant frequency relating to each incident direction as shown in Fig. 2(f); effectively surpassing the single-channel constraint typically exhibited by conventional arrays.

III. EXPERIMENTAL ARRAY PERFORMANCE

The theoretical framework established earlier is validated through an experimental performance evaluation of the proposed STP-PWD phased array. The array is constructed out of 12 PWDs (Manufacturer: Steminc Inc., Model: SMD05T04R111WL) forming 2 spatial unit cells which are epoxy-bonded (Manufacturer: 3M, Model: Scotch-Weld DP 270) to the center of an $1066 \times 1066 \times 1.27$ mm^3 Aluminum plate (5052 Aluminum Alloy). The complete setup is shown in Fig. 3 (see Supplementary Note 5 for details). Note that the piezoelectric discs used in this work are capable of inducing in-plane radial strain which can generate the required antisymmetric Lamb waves accordingly. Additionally, to minimize the amplitude of reflections, boundaries were covered with the damping material (Blu-Tack adhesive) to form a perfectly matched layer. In transmission, the elements of the array were excited using individual phase-modulated amplified harmonic signals with a frequency of $\omega/2\pi = 3$ kHz. The excitations were generated by a custom driver controlled with a MATLAB code which utilizes the Data Acquisition Toolbox. The phase-modulated signals were created digitally and then converted to analog signals using a D2A converter. The analog signals were amplified and tuned to generate a peak-to-peak voltage of $V_{pp} \cong 14$V for each channel. In order to visualize the elastic wave propagation, the out-of-plane velocity wave field was captured using a Polytec PSV-500 scanning laser Doppler vibrometer (SLDV), which is triggered from MATLAB's command line to ensure synchronized measurements with respect to the excitation signal. The measurements were taken over a scanning area of 1000×500 mm^2 with a resolution of 12 points per wavelength (12pt/λ) and a sampling frequency of 100 kHz. The top panel of Fig. 4 presents the experimentally measured out-of-plane velocity wave field at $t = 0.001$ seconds generated by the phased array in transmission corresponding to a modulation depth of $\delta = 1.5$ (left) and $\delta = 2.4$ (right). The close-up insets in both figures show the recorded measurements in both frequency and time-domain for the three sensor locations depicted by the red, blue and green discrete markers for the up-converted, fundamental and down-converted harmonics, respectively. The experimentally recorded wave fields as well as the frequency content of the generated harmonics show good agreement with predictions, i.e., both theoretical and simulation results presented in Fig. 2 for both modulation depths; thus validating the behavior of the array in transmission mode (see Supplementary Movies 1 and 2 for the transient response in transmission mode). In reception, incident plane waves with an excitation frequency of $\tilde{\omega}/2\pi = 3$ kHz were generated using two arrays of piezoelectric discs which are bonded to the plate at angles of 41° and -41° (principal reception directions), respectively, with respect to the broadside. Once the incident wave reaches the STP-PWD phased array, the signals are recorded and post-processed to augment the STP phase modulation and then summed up to yield the net voltage signal. The bottom panel of Fig. 4 shows incoming wave fields incident upon the STP-PWD array from the principal reception directions: $\tilde{\theta}_{\mathrm{A},+1}$ (left) and $\tilde{\theta}_{\mathrm{A},-1}$ (right). In these figures, insets in the top left corner depict the post-processed modulated signals collected from each channel of the STP-PWD phased array in light pink (background lines) and the collected voltage $\tilde{v}(t)$ in magenta (foreground line). The collected voltage signal from the output port is the total sum of the individual modulated signals which can be analyzed to estimate the direction of arrival. The top right insets show the collected voltage (unmodulated) from the first (navy-blue) and last (maroon) elements of the phased array. An inherent phase shift can be observed due to the direction of incidence of the incoming wave. For example, when the direction of incidence is $\tilde{\theta}_{\mathrm{A0},+1}$ ($\tilde{\theta}_{\mathrm{A0},-1}$), the waves first reach the first (last) piezo-disc before reaching the last (first) one which explains the phase shift in the recorded signals. The bottom insets show the normalized FFT amplitude of the collected signal at the output port, indicating a frequency conversion, and is utilized to estimate the direction of arrival of the incident wave. These results validate the theoretical findings presented in Fig. 2 for the behavior of the array in reception mode (see Supplementary Movies 3 and 4 for the transient response during reception).

IV. WAVE BEAMING AND MULTI-CHANNEL NONRECIPROCITY

To demonstrate the capabilities of the STP-PWD array to instigate some form of wave nonreciprocity, we examined its response in transmission mode to its counterpart when operating under a time-reversed signal. Figure 5(a) shows the transmission channels of the array operating at $\delta = 1.5$ as a result of an input voltage carrying a fundamental frequency ω. As anticipated, three distinct waves with different frequencies are observed, each propagating in its respective principal transmission direction, $\theta_{\mathrm{A},q}$. We then examined the array's output when a time-reversed version of either of these transmitted waves are incident upon the array (i.e., incident plane waves with the same frequency traveling in reverse direction towards the array, as shown in Fig. 5(b)). The angle of incidence associated with the fundamental wave ω is θ_{A}, which is received with the same frequency as shown in the middle panel of Fig. 5(b); reasserting the reciprocal behavior within the array's fundamental channel. A comparison between the frequency content of the output voltage signal in reception of each of the cases with the input signal in transmission (ω) reveals the nonreciprocal nature of the proposed array. On the other hand, the angle of incidence associated with the up-converted wave is $\theta_{\mathrm{A},+1}$, which is received with a predominant frequency of $\omega^{(+2)}$ (leftmost panel of Fig. 5(b)). This double up-conversion is a direct manifestation of the induced bias

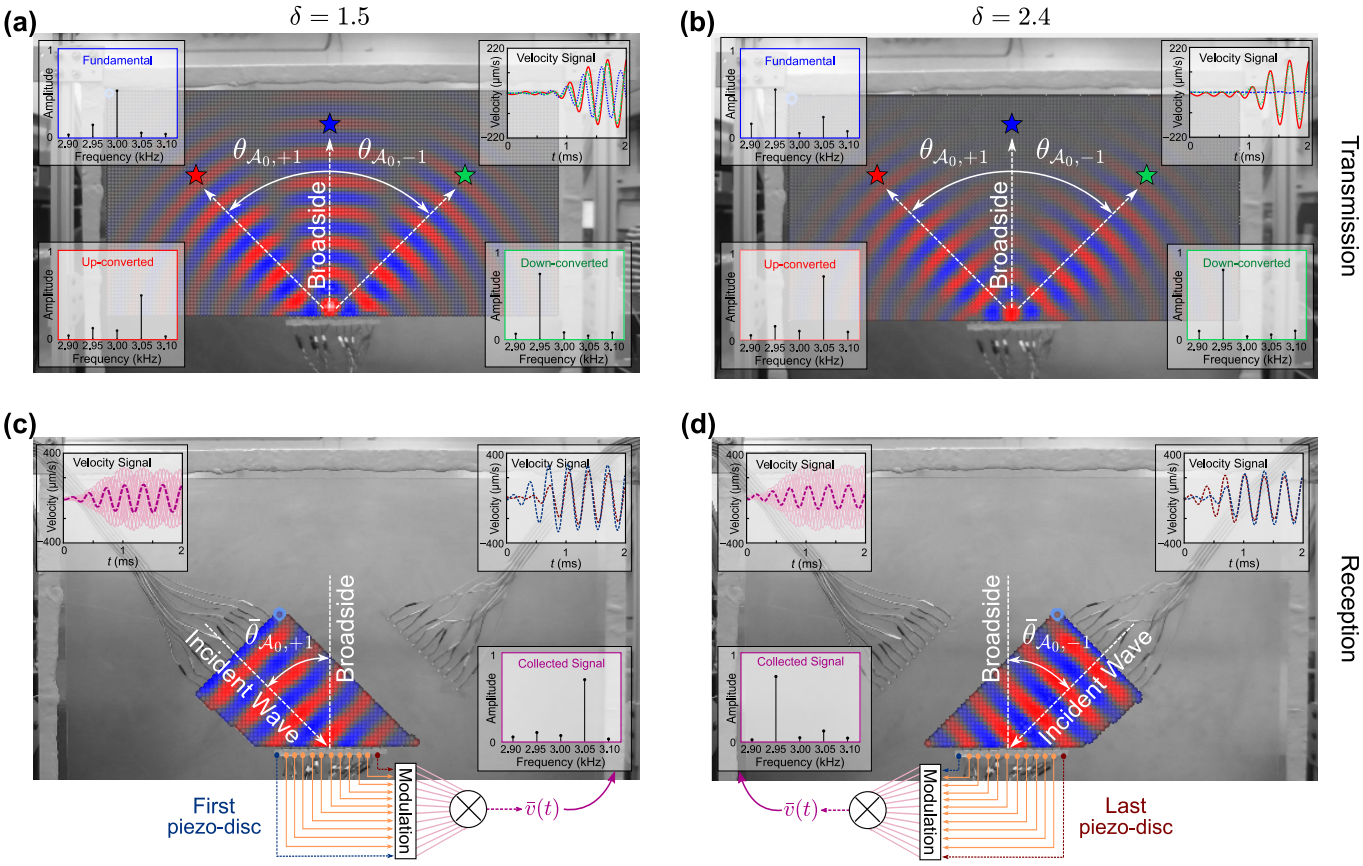

FIG. 4. **Experimental performance of the dynamic array.** (a,b) Out-of-plane velocity wave field for $\delta = 1.5$ and $\delta = 2.4$ at $t = 0.001$ seconds. In (a) and (b), the insets show time and frequency domain measurements at sensor locations indicated by the red, blue and green markers which are placed at a radial distance of 450 mm from the center of the plate at principal transmission directions. (c,d) Out-of-plane velocity wave fields of the generated incident waves approaching the array from principal reception directions. In (c) and (d), the top-left insets shows the post-processed individually modulated signals for each of the channels in light pink and the collected voltage signal in magenta. The top-right insets show the unmodulated signal from the first (navy-blue) and last (maroon) elements of the phased array. The bottom insets shows the normalized FFT amplitude of the collected voltage signal at the output port. All parameters are same as those used in Fig. 2.

in the system. A similar pattern can be observed for the down-converted wave which at reception shows a spectrum dominated by $\omega^{(-2)}$ (rightmost panel of Fig. 5(b)). The same conclusions pertaining to the array's behavior in reception mode can be arrived at using Eq. (8), as detailed in Supplementary Note 4. Figure 5(c) illustrates the characteristics of the signal at different stages of the reception process in both frequency (right panel) and time (left panel) domains. The received signal is fed through the STP phase-shifters and finally collected at the output port.

Another way to quantify the reciprocity of the system (or lack thereof) is via the extent to which radiation and reception patterns are identical within a given array. The STP-PWD array is capable of breaking reciprocity by introducing different principal transmission and reception directions. We examine the antisymmetric Lamb waves and define $\Delta\theta_{\mathrm{A},q}$ as the difference between the principal transmission and reception angles, i.e., $\Delta\theta_{\mathrm{A},q} = \theta_{\mathrm{A},q} - \tilde{\theta}_{\mathrm{A},q}$. For the special case corresponding to $\tilde{\omega} = \omega$, $\Delta\theta_{\mathrm{A},q}$ is nonzero for all values of $q \neq 0$ and is proportional to the ratio of ω_m/ω. As anticipated, $\Delta\theta_{\mathrm{A},q}$ vanishes at $q = 0$, which is reminiscent of the behavior of conventional phased arrays. To further illustrate, Fig. 5(d) demonstrates the effect of the modulation frequency ratio ω_m/ω on both radiation and reception patterns of an STP-PWD phased array; which perfectly coincide at $\omega_m/\omega = 0$ (demonstrating a fully-reciprocal response). As the modulation frequency ratio increases, the difference between the principal angles becomes more stark since $\Delta\theta_{\mathrm{A},q}$ takes on nonzero values for up- and down-converted waves. In effect, the dissimilarity between radiation and reception patterns, and consequently the degree of nonreciprocity, becomes stronger with faster modulation.

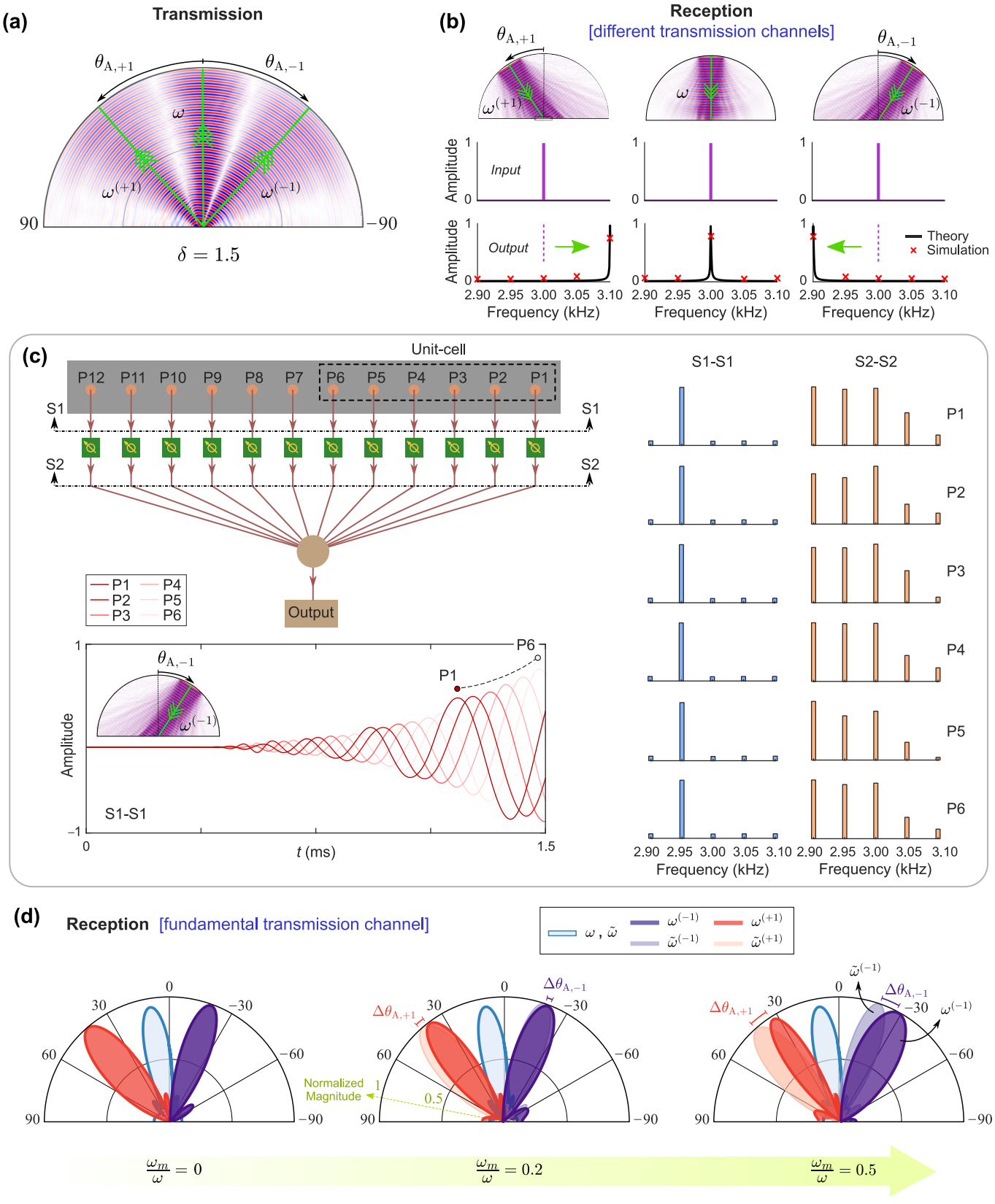

FIG. 5. **Nonreciprocal wave beaming in the STP-PWD phased array.** (a) Transmission channels as a result of an input voltage signal with frequency of ω. (b) Reception process and normalized FFT amplitudes (as predicted from both theory and simulations) of received signal at the output port corresponding to different transmission channels. (c) Characteristics of the received signal in different stages of the reception process. (d) Effect of temporal modulation speed on the radiation and reception patterns of the STP-PWD phased array. The parameter used are as follows: $\omega/2\pi = \tilde{\omega}/2\pi = 3$ kHz, $\omega^{(+1)}/2\pi = \tilde{\omega}^{(+1)}/2\pi = 3.05$ kHz, $\omega^{(-1)}/2\pi = \tilde{\omega}^{(-1)}/2\pi = 2.95$ kHz, $\kappa_c = 5.4113\pi$, $\kappa_m = 15.4821\pi$ and $\delta = 1.5$.

V. CONCLUSION

In summary, a conventional PWD phased array transmits guided waves in a desired direction by augmenting the individual voltage signals inputted to each array element by a static phase gradient κ_c. For the same set of parameters, it can *only* listen for guided waves arriving from the same exact direction. In contrast, in an STP-PWD phased array, the individual input voltage signals for the PWDs are augmented with a dynamically-varying phase angle, enabling an intentional breakage of elastoacoustic reciprocity and establishing independent (and tunable) radiation and reception patterns, while simultaneously allowing for multiple-channel operation in both transmission and reception regimes.

ACKNOWLEDGMENTS

The authors acknowledges support of this work from the US National Science Foundation through awards no. 1847254 (CAREER) and 1904254, as well as support from the University at Buffalo (SUNY) through the Buffalo Blue Sky Program.

AUTHOR CONTRIBUTIONS

M.M., R.A., and M.A.A. carried out the analysis and performed the calculations. M.M. and R.A. planned the experiments, constructed the setup, and conducted the measurements. All authors contributed to interpretation of the results. A.A. and M.N. supervised the project. The paper was written with input from all authors.

[1] V. Giurgiutiu, *Structural health monitoring: with piezoelectric wafer active sensors* (Elsevier, 2007).
[2] J. He, D. C. Rocha, and P. Sava, Guided wave tomography based on least-squares reverse-time migration, Structural Health Monitoring **19**, 1237 (2020).
[3] Q. Chen, K. Xu, and D. Ta, High-resolution lamb waves dispersion curves estimation and elastic property inversion, Ultrasonics , 106427 (2021).
[4] M. Mazzotti, C. Sugino, E. Kohtanen, A. Erturk, and M. Ruzzene, Experimental identification of high order lamb waves and estimation of the mechanical properties of a dry human skull, Ultrasonics **113**, 106343 (2021).
[5] C. He, X. Zhang, Y. Lu, B. Wu, and Y.-C. Lee, Sound fields radiated from a linear phased array based on analytical solutions of transient elastic waves, Wave Motion **73**, 86 (2017).
[6] Z. Tian and L. Yu, Elastic phased diffraction gratings for manipulation of ultrasonic guided waves in solids, Physical Review Applied **11**, 024052 (2019).
[7] X. Cao, C. Jia, H. Miao, G. Kang, and C. Zhang, Excitation and manipulation of guided shear-horizontal plane wave using elastic metasurfaces, Smart Materials and Structures **30**, 055013 (2021).
[8] X. Qing, W. Li, Y. Wang, and H. Sun, Piezoelectric transducer-based structural health monitoring for aircraft applications, Sensors **19**, 545 (2019).
[9] T. Sun, F. Tasnim, R. T. McIntosh, N. Amiri, D. Solav, M. T. Anbarani, D. Sadat, L. Zhang, Y. Gu, M. A. Karami, *et al.*, Decoding of facial strains via conformable piezoelectric interfaces, Nature Biomedical Engineering **4**, 954 (2020).
[10] T. Omirou, A. Marzo, S. A. Seah, and S. Subramanian, Levipath: Modular acoustic levitation for 3d path visualisations, in *Proceedings of the 33rd Annual ACM Conference on Human Factors in Computing Systems* (2015) pp. 309–312.
[11] A. Marzo, S. A. Seah, B. W. Drinkwater, D. R. Sahoo, B. Long, and S. Subramanian, Holographic acoustic elements for manipulation of levitated objects, Nature communications **6**, 1 (2015).
[12] K. F. Braun, Electrical oscillations and wireless telegraphy, Nobel Lecture, December **11**, 226 (1909).
[13] R. Mailloux, *Phased Array Antenna Handbook, Third Edition*, Artech House antennas and electromagnetics analysis library (Artech House Publishers, 2017).
[14] S.-C. Wooh and Y. Shi, Optimum beam steering of linear phased arrays, Wave motion **29**, 245 (1999).
[15] C. V. Poulton, A. Yaacobi, D. B. Cole, M. J. Byrd, M. Raval, D. Vermeulen, and M. R. Watts, Coherent solid-state lidar with silicon photonic optical phased arrays, Optics letters **42**, 4091 (2017).
[16] A. Hassanien and S. A. Vorobyov, Phased-mimo radar: A tradeoff between phased-array and mimo radars, IEEE Transactions on Signal Processing **58**, 3137 (2010).
[17] T. M. Rynne, J. F. Spadaro, J. L. Iovenitti, J. P. Dering, and D. G. Hill, Phased array approach to retrieve gases, liquids, or solids from subaqueous geologic or man-made formations (1998), uS Patent 5,826,653.
[18] L. Yu and V. Giurgiutiu, In situ 2-d piezoelectric wafer active sensors arrays for guided wave damage detection, Ultrasonics **48**, 117 (2008).
[19] L. Yu and V. Giurgiutiu, In-situ optimized pwas phased arrays for lamb wave structural health monitoring, Journal of mechanics of materials and structures **2**, 459 (2007).
[20] A. Purekar, D. Pines, S. Sundararaman, and D. Adams, Directional piezoelectric phased array filters for detecting damage in isotropic plates, Smart Materials and Structures **13**, 838 (2004).
[21] Q. Huan, M. Chen, Z. Su, and F. Li, A high-resolution structural health monitoring system based on sh wave piezoelectric transducers phased array, Ultrasonics **97**, 29 (2019).
[22] X. Zhang, W. Zhou, H. Li, and Y. Zhang, Guided wave-based bend detection in pipes using in-plane shear piezoelectric wafers, NDT & E International **116**, 102312 (2020).
[23] M. Vahedi, R. Ardestani, and S. M. Zahrai, Sensitivity analysis of tubular-web reduced beam section connections under cyclic loading, International Journal of Steel Structures , 1 (2020).

[24] J. Hu, H. Peng, X. Yao, T. Liu, P. Lu, and C. Zhao, An investigation to the design of high-precision wind sensing device based on piezoelectric array, Transactions of the Institute of Measurement and Control **42**, 840 (2020).

[25] Y. Ohara, M. C. Remillieux, T. Onuma, K. Tsunoda, T. Tsuji, and T. Mihara, Toward an ultra-high resolution phased-array system for 3d ultrasonic imaging of solids, Applied Physics Letters **117**, 111902 (2020).

[26] Y. Ohara, S. Yamamoto, T. Mihara, and K. Yamanaka, Ultrasonic evaluation of closed cracks using subharmonic phased array, Japanese Journal of Applied Physics **47**, 3908 (2008).

[27] O. Buck, W. Morris, and J. M. Richardson, Acoustic harmonic generation at unbonded interfaces and fatigue cracks, Applied Physics Letters **33**, 371 (1978).

[28] S. Biwa, S. Nakajima, and N. Ohno, On the acoustic nonlinearity of solid-solid contact with pressure-dependent interface stiffness, J. Appl. Mech. **71**, 508 (2004).

[29] H. Kazari, M. Kabir, A. Mostavi, and D. Ozevin, Multifrequency piezoelectric micromachined ultrasonic transducers, IEEE Sensors Journal **19**, 11090 (2019).

[30] Y. Ohara, H. Nakajima, T. Tsuji, and T. Mihara, Nonlinear surface-acoustic-wave phased array with fixed-voltage fundamental wave amplitude difference for imaging closed cracks, NDT & E International **108**, 102170 (2019).

[31] J. Cheng, J. N. Potter, A. J. Croxford, and B. W. Drinkwater, Monitoring fatigue crack growth using nonlinear ultrasonic phased array imaging, Smart Materials and Structures **26**, 055006 (2017).

[32] S. Haupert, G. Renaud, and A. Schumm, Ultrasonic imaging of nonlinear scatterers buried in a medium, NDT & E International **87**, 1 (2017).

[33] Y. Ohara, H. Nakajima, S. Haupert, T. Tsuji, and T. Mihara, Imaging of three-dimensional crack open/closed distribution by nonlinear ultrasonic phased array based on fundamental wave amplitude difference, Japanese Journal of Applied Physics **59**, SKKB01 (2020).

[34] C. Bruno, A. Gliozzi, M. Scalerandi, and P. Antonaci, Analysis of elastic nonlinearity using the scaling subtraction method, Physical Review B **79**, 064108 (2009).

[35] J. Achenbach and J. Achenbach, *Reciprocity in elastodynamics* (Cambridge University Press, 2003).

[36] J. D. Adam, L. E. Davis, G. F. Dionne, E. F. Schloemann, and S. N. Stitzer, Ferrite devices and materials, IEEE Transactions on Microwave Theory and Techniques **50**, 721 (2002).

[37] D. L. Sounas and A. Alù, Non-reciprocal photonics based on time modulation, Nature Photonics **11**, 774 (2017).

[38] N. Antonellis, R. Thomas, M. Kats, I. Vitebskiy, and T. Kottos, Nonreciprocity in photonic structures with phase-change components, Physical Review Applied **11**, 024046 (2019).

[39] C. Sanavio, V. Peano, and A. Xuereb, Nonreciprocal topological phononics in optomechanical arrays, Physical Review B **101**, 085108 (2020).

[40] X. Zhu, J. Li, C. Shen, X. Peng, A. Song, L. Li, and S. A. Cummer, Non-reciprocal acoustic transmission via space-time modulated membranes, Applied Physics Letters **116**, 034101 (2020).

[41] L. Shao, W. Mao, S. Maity, N. Sinclair, Y. Hu, L. Yang, and M. Loncar, Nonreciprocal acoustic transmission using lithium niobate parity-time-symmetric resonators, in *CLEO: QELS_Fundamental Science* (Optical Society of America, 2020) pp. FTh4Q–2.

[42] R. Fleury, D. L. Sounas, C. F. Sieck, M. R. Haberman, and A. Alù, Sound isolation and giant linear nonreciprocity in a compact acoustic circulator, Science **343**, 516 (2014).

[43] Z. Yang, F. Gao, X. Shi, X. Lin, Z. Gao, Y. Chong, and B. Zhang, Topological acoustics, Physical review letters **114**, 114301 (2015).

[44] R. Fleury, D. Sounas, M. R. Haberman, and A. Alu, Nonreciprocal acoustics, Acoustics Today **11**, 14 (2015).

[45] A. Sasmal, N. Geib, B.-I. Popa, and K. Grosh, Broadband nonreciprocal linear acoustics through a non-local active metamaterial, New Journal of Physics **22**, 063010 (2020).

[46] M. Attarzadeh, S. Maleki, J. Crassidis, and M. Nouh, Non-reciprocal wave phenomena in energy self-reliant gyric metamaterials, The Journal of the Acoustical Society of America **146**, 789 (2019).

[47] H. Nassar, B. Yousefzadeh, R. Fleury, M. Ruzzene, A. Alù, C. Daraio, A. N. Norris, G. Huang, and M. R. Haberman, Nonreciprocity in acoustic and elastic materials, Nature Reviews Materials , 1 (2020).

[48] Y. Chen, X. Li, G. Hu, M. R. Haberman, and G. Huang, An active mechanical willis meta-layer with asymmetric polarizabilities, Nature communications **11**, 1 (2020).

[49] A. Palermo, P. Celli, B. Yousefzadeh, C. Daraio, and A. Marzani, Surface wave non-reciprocity via time-modulated metamaterials, Journal of the Mechanics and Physics of Solids **145**, 104181 (2020).

[50] M. Attarzadeh, J. Callanan, and M. Nouh, Experimental observation of nonreciprocal waves in a resonant metamaterial beam, Physical Review Applied **13**, 021001 (2020).

[51] D.-W. Wang, H.-T. Zhou, M.-J. Guo, J.-X. Zhang, J. Evers, and S.-Y. Zhu, Optical diode made from a moving photonic crystal, Physical review letters **110**, 093901 (2013).

[52] E. Riva, M. Di Ronco, A. Elabd, G. Cazzulani, and F. Braghin, Non-reciprocal wave propagation in discretely modulated spatiotemporal plates, Journal of Sound and Vibration **471**, 115186 (2020).

[53] A. M. Shaltout, V. M. Shalaev, and M. L. Brongersma, Spatiotemporal light control with active metasurfaces, Science **364** (2019).

[54] X. Wang, A. Díaz-Rubio, H. Li, S. A. Tretyakov, and A. Alù, Theory and design of multifunctional space-time metasurfaces, Physical Review Applied **13**, 044040 (2020).

[55] A. E. Cardin, S. R. Silva, S. R. Vardeny, W. J. Padilla, A. Saxena, A. J. Taylor, W. J. Kort-Kamp, H.-T. Chen, D. A. Dalvit, and A. K. Azad, Surface-wave-assisted nonreciprocity in spatio-temporally modulated metasurfaces, Nature communications **11**, 1 (2020).

[56] V. Tiukuvaara, T. J. Smy, and S. Gupta, Floquet analysis of space-time modulated huygens' metasurfaces with lorentz dispersion, arXiv preprint arXiv:2007.07063 (2020).

[57] J. Zang, A. Alvarez-Melcon, and J. Gomez-Diaz, Nonreciprocal phased-array antennas, Physical review applied **12**, 054008 (2019).

[58] C. A. Balanis, *Antenna theory: analysis and design* (John wiley & sons, 2016).

[59] R. Adlakha, M. Moghaddaszadeh, M. A. Attarzadeh, A. Aref, and M. Nouh, Frequency selective wave beaming in nonreciprocal acoustic phased arrays, Scientific reports

10, 1 (2020).
[60] R. Adlakha, M. Moghaddaszadeh, M. Attarzadeh, A. Aref, and M. Nouh, A linear acoustic phased array for nonreciprocal transmission and reception, in *ASME International Mechanical Engineering Congress and Exposition*, Vol. 84478 (American Society of Mechanical Engineers, 2020) p. V001T01A016.
[61] C. Rasmussen, L. Quan, and A. Alù, Acoustic nonreciprocity, Journal of Applied Physics **129**, 210903 (2021).
[62] See supplemental material at [url will be inserted by publisher] for extended methods and videos.
[63] J. L. Rose, *Ultrasonic guided waves in solid media* (Cambridge university press, 2014).